



The effects of air gap reflections during air-coupled leaky Lamb wave inspection of thin plates



Zichuan Fan^{a,b}, Wentao Jiang^a, Maolin Cai^b, William M.D. Wright^{a,*}

^a School of Engineering – Electrical and Electronic Engineering, University College Cork, Cork, Ireland

^b School of Automation Science and Electrical Engineering, Beihang University, Beijing, People's Republic of China

ARTICLE INFO

Article history:

Received 27 April 2015

Received in revised form 24 July 2015

Accepted 20 September 2015

Available online 26 September 2015

Keywords:

Air-coupled ultrasound

Leaky Lamb waves

Finite element method

Multiphysics modelling

Air-gap reflections

ABSTRACT

Air-coupled ultrasonic inspection using leaky Lamb waves offers attractive possibilities for non-contact testing of plate materials and structures. A common method uses an air-coupled pitch-catch configuration, which comprises a transmitter and a receiver positioned at oblique angles to a thin plate. It is well known that the angle of incidence of the ultrasonic bulk wave in the air can be used to preferentially generate specific Lamb wave modes in the plate in a non-contact manner, depending on the plate dimensions and material properties. Multiple reflections of the ultrasonic waves in the air gap between the transmitter and the plate can produce additional delayed waves entering the plate at angles of incidence that are different to those of the original bulk wave source. Similarly, multiple reflections of the leaky Lamb waves in the air gap between the plate and an inclined receiver may then have different angles of incidence and propagation delays when arriving at the receiver and hence the signal analysis may become complex, potentially leading to confusion in the identification of the wave modes. To obtain a better understanding of the generation, propagation and detection of leaky Lamb waves and the effects of reflected waves within the air gaps, a multiphysics model using finite element methods was established. This model facilitated the visualisation of the propagation of the reflected waves between the transducers and the plate, the subsequent generation of additional Lamb wave signals within the plate itself, their leakage into the adjacent air, and the reflections of the leaky waves in the air gap between the plate and receiver. Multiple simulations were performed to evaluate the propagation and reflection of signals produced at different transducer incidence angles. Experimental measurements in air were in good agreement with simulation, which verified that the multiphysics model can provide a convenient and accurate way to interpret the signals in air-coupled ultrasonic inspection using leaky Lamb waves.

© 2015 Elsevier B.V. All rights reserved.

1. Introduction

Air-coupled ultrasonic testing provides an attractive couplant-free and non-contact alternative to immersion or contact methods of ultrasonic non-destructive testing. Because of the non-contact nature of transduction and improvements in transducer efficiency, it offers possibilities in many applications such as in-line inspection of materials, management of manufacturing processes, and quality assurance of the products [1–6].

In the cases concerning plate materials and structures, air-coupled ultrasonic testing can be implemented by utilising leaky Lamb waves and a pitch-catch configuration. Relevant investigations have been done in recent years for applications such as materials characterisation, defect detection and tomographic imaging

[7–15]. Although most of these previous works were focused on the experimental systems, the availability of simulation models is important for a good understanding of the observed ultrasonic effects [15–17]. Air-coupled inspection is still restricted in use by the energy loss due to the large impedance mismatch at the interface of the solid and the air. Accurate numerical simulation models are required to facilitate the design and improvement of the experimental systems [18].

Castaigns and Hosten [13] applied a transfer matrix method to simulate the propagation of leaky, guided modes in stratified plates made of anisotropic, viscoelastic materials. Kazys et al. [14] implemented the 2D numerical simulations of wave interaction with the defect using Wave2000 software. Ramadas et al. [15] used the finite element package ANSYS to model the interaction of air-coupled Lamb waves with delaminations in composite plates. Other work by Hosten and Biateau [16] has looked at finite element modelling for computing the wave propagation in air and

* Corresponding author.

E-mail address: bill.wright@ucc.ie (W.M.D. Wright).

the dynamic equations of equilibrium inside the plate. Later, Delrue et al. [17] investigated two distinctive methods for ultrasonic imaging of the defect. The first one was based on a ray tracing (shadow) approach, and the second one used a spectral solution implemented with COMSOL. Dobie et al. [18] applied a linear systems approximation to simulate transducer behaviour, and the local interaction simulation approach for wave propagation in the structure. Recently, Vilpisauskas and Kazys [19] introduced an analytical model for an isotropic single layer plate combined with the Impulse Response Method for calculating acoustic pressure.

Although many simulation methods have been investigated, these previous studies have concentrated on modelling the propagation of Lamb waves within the plates of various materials or the behaviour of specific transducer types. However, little attention has been paid to the effects of the reflections in the air gap between the transducers and the plate, which is the focus of the current study.

It is well known that the excitation of specific Lamb wave modes may be achieved by careful selection of the ultrasonic frequency and angle of incidence to match the plate thickness and material. As many air-coupled transducers are quite large and need to be close to the test surface to minimise attenuation in air, the significant amounts of ultrasonic energy reflected from the surface of the plate may also reflect again from the surface of the transducer back towards the plate at a different angle of incidence, producing a delayed secondary Lamb wave source. Similarly, reflections of the leaky Lamb waves in the air gap between the plate and the receiver may produce other instances of the received signal. These additional air-gap reflections may thus produce more complex signals and affect air-coupled inspection signal analysis. Few studies of air-coupled inspection using leaky Lamb waves have used multiphysics modelling, which is a convenient and accurate method to allow detailed study of the wave behaviour, and can include the configuration of the transducers, the propagation of waves in the plate, and any influences due to multiple reflections between the plate and the transducers. A relevant experimental study supported by the multiphysics modelling will thus be useful to reveal the reflection effects and improve air-coupled inspection systems.

In this paper, we investigate multiphysics modelling using a finite element method of a two-sided pitch-catch transducer configuration, where the transmitter and receiver are positioned at oblique angles on opposite sides of a simple test plate. An ultrasonic wave, generated in air by the transmitter, enters the plate, converts to a Lamb wave and leaks energy into the coupling air as it propagates. Depending on the air gap between the transducers and the plate, and the angle of incidence, reflections of the transmitted wave and the leaky Lamb waves may exist in the air gap between the transducers and the plate and produce secondary signals. All the wave behaviour was modelled in COMSOL Multiphysics.

In Section 2 of this paper, details of the multiphysics modelling are given. Section 3 covers the results and analysis of the numerical simulations. The relative intensity of the air-coupled Lamb waves excited by different incidence angles is also evaluated. Experimental measurements are observed and discussed in Section 4, and compared with the results from simulation. Conclusions about this method are drawn in Section 5.

2. Multiphysics modelling

The purpose of this study was to concentrate on the reflected signals in the air gaps between the transducers and the plate rather than the behaviour of the transducer or the properties of the plate

used, so the choice of transducer type and plate material was rather arbitrary. To reduce unnecessary model complexity, the mechanism of operation of the transducer itself was not included in the simulation, and the plate material was chosen to be a homogenous polymer (polycarbonate) to (i) simplify the signals produced during leaky Lamb wave propagation and (ii) to ensure a relatively low impedance mismatch to aid experimental production and detection of the signals. However, it should be pointed out that the modelling approach used here can be extended to include specific transducer types (piezoelectric, capacitive, etc.) and more complicated plate structures and materials, such as metals and fibre-reinforced composites.

To determine the Lamb wave modes present in the plate, the velocity dispersion curves may be readily derived from the Rayleigh–Lamb frequency equations [20]. It is well known that careful selection of the correct ultrasonic frequency to match the thickness and material of the plate can restrict the modes that will propagate. Fig. 1 shows the theoretical dispersion curves for the first six antisymmetric and symmetric modes in polycarbonate, where it is clear that, for frequency-thickness products of less than 0.5 MHz mm, only the zero-order modes A_0 and S_0 can exist, and that at frequency-thickness products of less than 0.2 MHz mm there is high A_0 dispersion but low S_0 dispersion. Hence, a frequency of 100 kHz in a polycarbonate plate of thickness 1 mm to give a frequency-thickness product of 0.1 MHz mm was chosen to further simplify this preliminary study.

Multiphysics modelling aims to be a closer representation of the reality of the physical test. The implementation here is based on a finite element method using COMSOL Multiphysics, and contains the following steps. First, the geometry of the problem was established. In this study, a two-dimensional representation of the experiment was set up, and subdivided into different subdomains (the air, the plate and the transducers). Then the governing equations were defined for each subdomain. Boundary conditions between different subdomains were specified. In order to get an accurate solution, triangular mesh elements were chosen and then the optimum mesh size of the model was determined (the total number of domain elements was 411,986). Finally, before running the time dependent simulations by using a direct (segregated) solver, an appropriate time step was chosen.

2.1. Geometry

The basic geometry of the model is shown in Fig. 2. The plate used was polycarbonate with the following properties: length

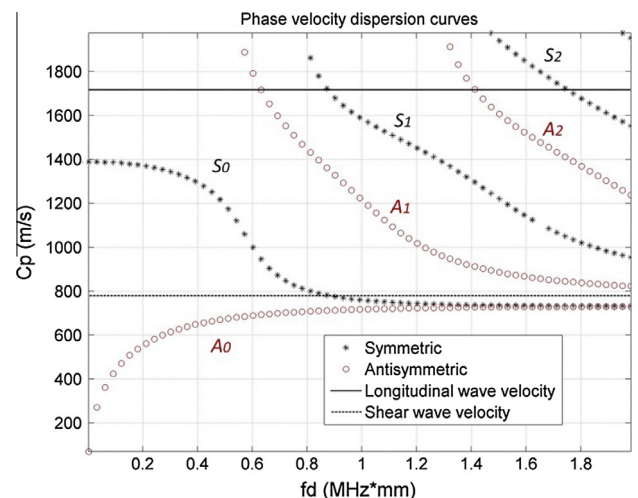


Fig. 1. Phase velocity dispersion curves of the first six symmetric and antisymmetric modes in polycarbonate.

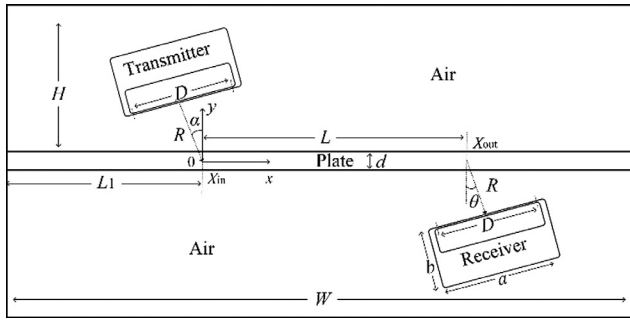


Fig. 2. Schematic diagram of the modelling geometry.

$W = 500$ mm, thickness $d = 1$ mm, Young's modulus $E = 2.0$ GPa, density $\rho = 1200$ kg/m³, Poisson's ratio $\nu = 0.37$. There were air domains with a height $H = 70$ mm above and below the plate. The transmitter with an active diameter of $D = 38$ mm was located such that the centre of its face was at a radius $R = 30$ mm from the entry point in the plate and deflected by the incidence angle, α . It was thus possible to orientate the transmitter at any incidence angle from 0° to 55° in the model so that the generation and detection of specific Lamb wave modes could be optimised. The entry point X_{in} of the bulk wave and exit point X_{out} of the leaky waves were taken as the intersection of the transducer centre normals with the plate centreline and were separated by a distance $L = 250$ mm. The distance from the entry point to the left edge of the plate was $L_1 = 150$ mm. The receiver was located at the same radius $R = 30$ mm from the leaky exit point in the plate and inclined by the incidence angle θ . The overall transmitter and receiver dimensions were length $a = 40$ mm and height $b = 20$ mm. Thus, by maintaining the radius $R = 30$ mm, the angles of incidence α and θ could be varied from 0° to 55° without the edge of either transducer touching the plate and ensuring a constant propagation distance in air at the centreline intensity.

2.2. Governing equations and boundary conditions

To address the modelling of wave conversion occurring at the interface of air and plate, the Acoustic-Structure Interaction Module of COMSOL Multiphysics was used. This module connects the acoustic pressure variations in the fluid domain with the structural deformation in the solid domain by combining the pressure acoustics and solid mechanics interfaces [21].

The parameters of air were determined at standard atmospheric conditions. Wave behaviour in air may be described by the scalar wave equation, which provides a solution for the sound pressure as follows:

$$\nabla \cdot \left(\frac{1}{\rho_c} \nabla p \right) - \frac{1}{\rho_c c^2} \frac{\partial^2 p}{\partial t^2} = 0, \quad (1)$$

where p is the total acoustic pressure, ρ_c is the fluid density and c is the speed of sound.

For the acoustic-solid interaction, the boundary condition between the fluid and the solid includes a structural acceleration acting on the boundaries between the solid and the fluid. This makes the normal acceleration for the acoustic pressure on the boundary equal to the acceleration as follows:

$$\mathbf{n}_f \cdot \left(\frac{1}{\rho_c} \nabla p \right) = a_n, \quad (2)$$

where a_n is the normal acceleration of the solid and \mathbf{n}_f is the outward-pointing unit normal vector seen from inside the fluid domain.

A pressure load is acting on the boundaries where the fluid interacts with the solid, given by:

$$\sigma \cdot \mathbf{n}_s = p \cdot \mathbf{n}_s, \quad (3)$$

where σ is the surface stress of the solid, \mathbf{n}_s is the outward-pointing unit normal vector seen from inside the solid domain.

2.3. Mesh size

To obtain a small simulation error, a fine mesh should be chosen. However, the computational burden will be large if the mesh size is too small. Thus, an appropriate mesh size that could adequately resolve the waves was used. For COMSOL Multiphysics, at least 5 second-order mesh elements were recommended per wavelength [21]. Considering the centre frequency in the simulation was 100 kHz, and that the minimum wavelength in the air domain was 3.43 mm, the maximum mesh size in the air domain was set at 0.5 mm, i.e. 6.9 elements per wavelength. For the plate, a finer mesh with a maximum size of 0.25 mm was used. The minimum wavelength of the Lamb waves in the plate was approximately 4 mm, which gave 16 elements per wavelength in the solid domain. This mesh size ensured accurate simulation of Lamb waves propagating in the plate.

2.4. Time step

The time step used in the simulations should resolve the wave as well in the time domain as the mesh does in the spatial domain. If the time step is too large, the mesh will not be fully utilised. Conversely, the results will not be improved significantly with a longer solution time using smaller time steps. An appropriate time step can be calculated according to the mesh size. The relationship between mesh size and time step length is called the Courant Friedrichs Lewy (CFL) number [22], given by:

$$\text{CFL} = c \times \Delta t / h, \quad (4)$$

where Δt is the time step, c is the velocity and h is the mesh size. A CFL number of 0.2 has proven to be near optimal for the default second order mesh elements used in most simulations [22]. Hence, according to the mesh size of 0.25 mm and the maximum wave velocity (longitudinal wave) in the plate, a default time step of $0.05 \mu\text{s}$ was used.

3. Simulation and analysis

To generate the pressure wave in air, a time dependent boundary load was applied uniformly to the transducer surface. This appropriately simulates plane piston behaviour of the transducers without the need for directly modelling the transducer behaviour. The capacitive ultrasonic transducers used by several authors in air-coupled applications e.g. [5,8,11] have been shown to have plane piston behaviour, and will be used in the experimental study described later in Section 4. As shown in Fig. 3, the source was a smooth windowed sinusoid of 5 cycles in length with a centre frequency of 100 kHz, given by:

$$F(t) = F_0 \sin(2\pi ft) \cdot (\sin(2\pi ft/10))^2 \cdot (t < 5/f), \quad (5)$$

where $F_0 = 1$ N.

The receiver surface will be deformed by the leaky Lamb waves propagating in air, so the mean displacement normal to the surface was chosen as the received signal to represent the detection of the leaky Lamb wave. The sample rate for the signals output from the simulations was 2.5 MHz, and the total time simulated was 1 ms.

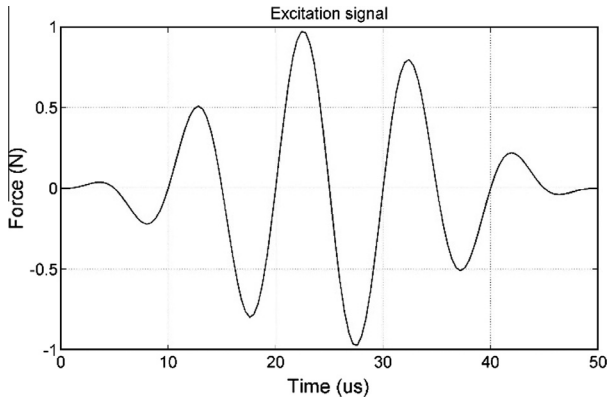


Fig. 3. Excitation signal.

3.1. Wave behaviour

The acoustic-solid interaction boundary condition used in simulations is close to a free boundary condition, so the Rayleigh-Lamb equations provide an approximation of the velocities. The phase and group velocities at low frequency-thickness products are illustrated in Fig. 4. It can be seen that a Lamb wave at 100 kHz travels in a 1 mm thick polycarbonate plate (i.e., at 0.1 MHz mm) with a group velocity of approximately 1380 m/s for the S_0 mode and of about 700 m/s for the A_0 mode, and a phase velocity of 1380 m/s for the S_0 mode and 430 m/s for the A_0 mode, respectively. Additionally, the refraction angles of leaky Lamb waves are determined by the phase velocities and Snell's Law. So the leaky Lamb waves at 100 kHz will propagate into the air from the plate at an angle of 14.4° for the S_0 mode and 52.9° for the A_0 mode.

Fig. 5 shows a snapshot of the wave fields in the plate and air domain obtained from the right-hand side of the model ($0 < x < L$) at a time of $300 \mu\text{s}$. In this simulation, the parameters of air were those determined at standard temperature and pressure, and the transmitter was at an incidence angle of 15° . The upper intensity scale in Fig. 5 is von Mises equivalent stress in N/m^2 in the plate, the lower intensity scale is air pressure in Pa (range changed for clarity).

From Fig. 5, it is clear from the intensity scales that the pressure wave leaking into the air from the antisymmetric A_0 mode on the

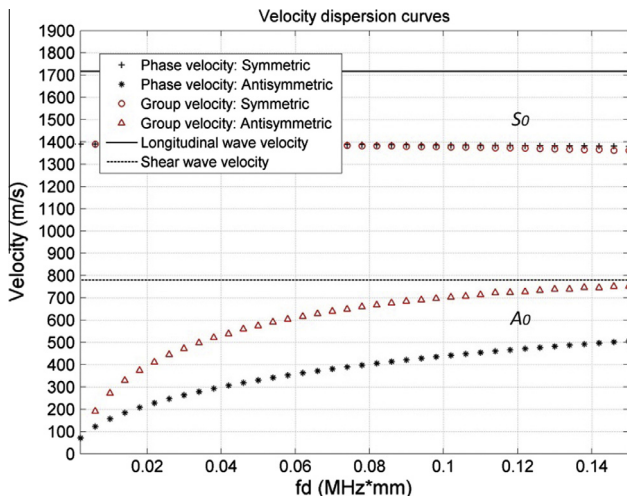


Fig. 4. Phase and group velocity dispersion curves at low frequency-thickness products.

left contains more energy than that leaking from the symmetric S_0 mode on the right, with a similar difference in energy for the Lamb waves propagating in the plate. It may also be seen in Fig. 5 that the pressure waves in air generated by the Lamb waves are leaking energy into the air at different angles with evidence of dispersion in the A_0 mode, as expected. The details of wave behaviour specified by particle movement in the plate and air may be further studied by using acceleration vector plots as shown in Fig. 6.

As can be seen in Fig. 6(a), for the S_0 mode, the particles of the plate move mostly in the x direction and move only slightly in the y direction with a small surface acceleration. As expected, the particle motion is mostly tensile and compressive along the plate axis for the symmetric mode. The leaky S_0 Lamb wave in the air also has a larger acceleration component in the y direction than in the x direction, resulting in a low angle of leakage. Please note that different magnification factors were used to view the vectors in the air and the plate domains.

In Fig. 6(b), for the A_0 mode, the particles of the plate are producing more surface tilt with a larger overall surface movement. The acceleration vectors vary significantly both in magnitude and direction. Compared with Fig. 6(a), a much smaller magnification factor is required to get the same visibility, because the movement of the plate in this mode is rather stronger than that in the symmetric mode. Additionally, it also shows that the wavelengths of the Lamb wave and the pressure wave in Fig. 6(b) are shorter than those in Fig. 6(a). The A_0 mode leaks into air at a large angle, as expected.

3.2. Intensity at different incidence angles

The intensity of leaky Lamb waves is highly related to the incidence angle as has been shown previously by numerous authors, e.g. [19,23]. The relationship between the angle and the signal intensity was also shown by the multiphysics model. By increasing the incidence angle of the transmitter from 10° to 55° , different incidence angles between the wave in the air and the plate were obtained. A point probe placed in the simulation at the centre of the receiver surface was used here to collect the pressure signal containing all the received energy for analysis. Another point probe was located at a distance $R/2$ from the zero point in the plate to the transmitter, which collects all the source signals emitting from the transmitter. The intensity of different leaky Lamb wave modes compared to the source signal is shown in Fig. 7. Only the leaky Lamb wave modes attributed to the first excitation are calculated.

From Fig. 7, the leaky A_0 Lamb wave mode has a minimum attenuation relative to the source signal at $50\text{--}55^\circ$, and maxima at 10° and 25° which are near the two critical angles of 11° and 26° for the shear wave and longitudinal wave velocities, respectively. The leaky S_0 Lamb wave mode has a minimum attenuation at 15° , and a maximum at 55° with a step change near the critical angle of 26° . Therefore, by adjusting the transmitter to the correct angle, a specific Lamb wave, in this case either the A_0 mode or the S_0 mode, can be preferentially excited and detected, and the other mode minimised.

3.3. Transducer-plate air gap reflections

For many air-coupled inspection applications, the transducers must be close to the sample under test to reduce the effects of attenuation in air, particularly at high frequencies and over long propagation paths. Air-coupled ultrasonic transducers are often large, and the pressure wave in air will thus reflect between the transducers and the plate if the gap is small enough. Thereby, multiple signals may be generated and detected due to the reflections in the air gaps. The relative angle of incidence of these reflections

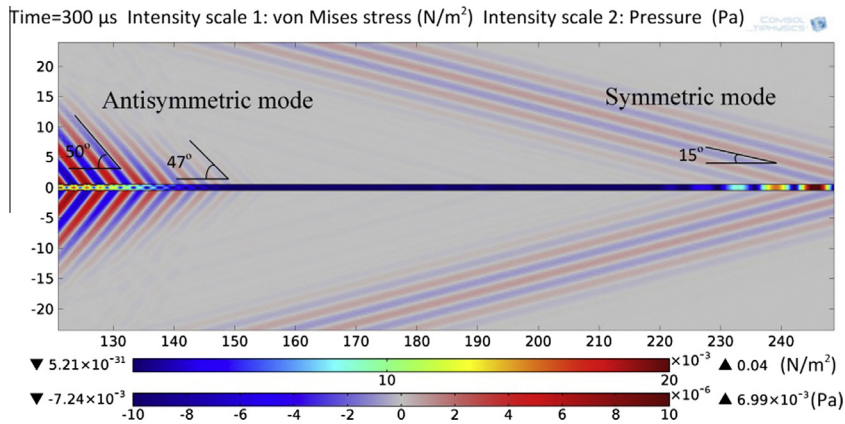


Fig. 5. Visualisation of Lamb wave propagation in the plate and leakage into air at a time of 300 μs.

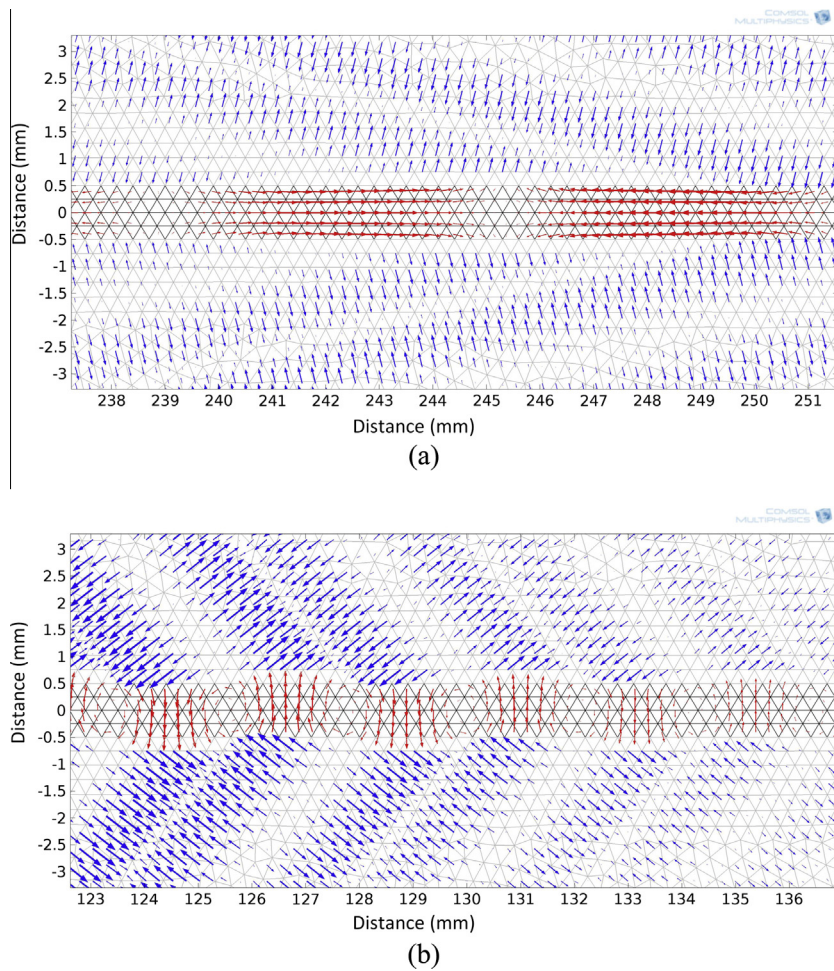


Fig. 6. Visualisation of particle movement at a time of 300 μs showing acceleration vectors in the air and in the plate; (a) Symmetric mode (magnification factors: 200 in air, 50 in the plate). (b) Antisymmetric mode (magnification factors: 50 in air, 50 in the plate).

may change and the amplitude of the Lamb waves produced and detected by subsequent reflected signals in the air gap may be higher than the original direct wave that first enters or leaves the plate. This may lead to misinterpretation of the measured signals, particularly if they are noisy, as the first wave received may not have necessarily the largest amplitude. On the transmitter side, additional Lamb waves may be excited by the reflected bulk wave. On the receiver side, the receiver may detect the reflected leaky

Lamb waves at an angle different from the original refraction angle. The mechanisms of these two kinds of reflection are illustrated schematically in Fig. 8.

In Fig. 8(a), for a transmitter placed near to a plate at an oblique angle, the pressure wave enters the plate at the incidence angle α , and then may reflect several times between the plate and the transmitter. Typically over 90% of the incident energy is reflected, depending on the specific acoustic impedance mismatch between

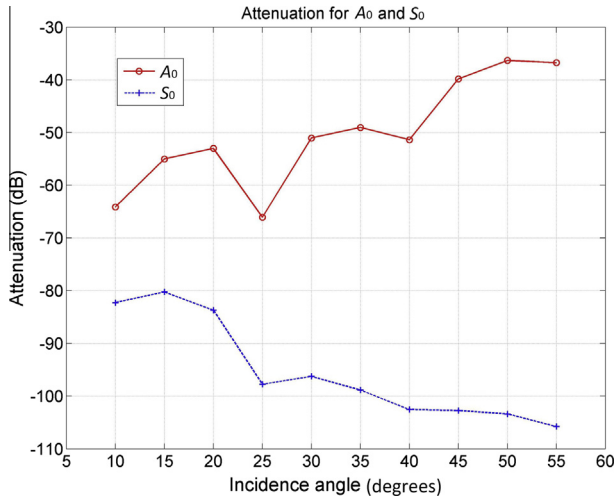


Fig. 7. Intensity dependency versus the incidence angle for simulations.

the plate and air, while a new incidence angle is then generated for the pressure wave after every reflection. In the case of two reflections, the new incidence angle α' may be calculated as follows:

$$\alpha' = 3\alpha, \tag{6}$$

$$R_{tr_max} = (0.5 \tan \alpha + \cot 2\alpha)D, \tag{7}$$

where R_{tr_max} defined by (7) provides the maximum value of the radius from the centre of the transmitter to the plate at which reflections will occur, i.e. if $R < R_{tr_max}$, reflections will exist between the plate and the transmitter.

In Fig. 8(b), the leaky Lamb wave propagates at the original refraction angle β , and reaches the receiver firstly at the angle of

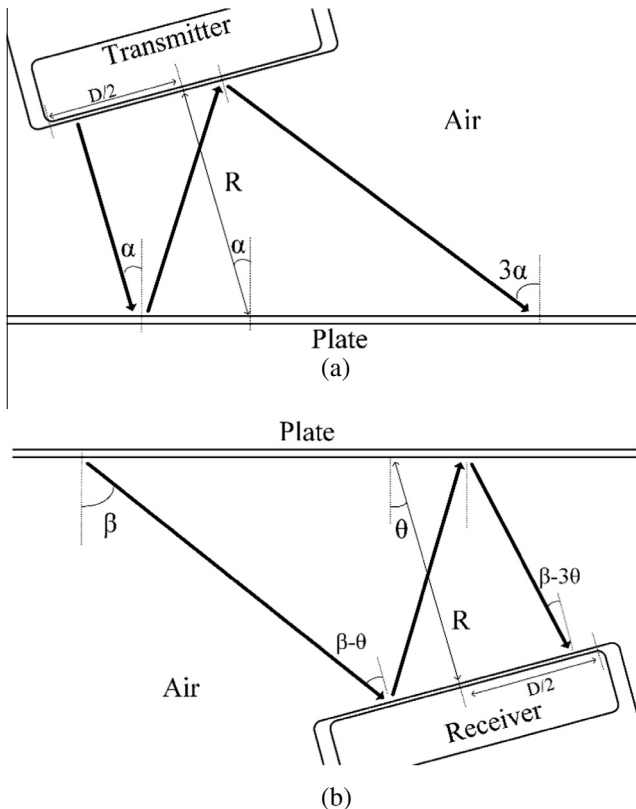


Fig. 8. Mechanisms of the reflection. (a) Reflection occurs in the transmitter side. (b) Reflection occurs in the receiver side.

$\beta - \theta$. The wave is first reflected by the receiver back towards the plate and then is reflected by the plate back towards the receiver at a new smaller angle, $\beta - 3\theta$. Similarly, the maximum value of the radius from the centre of the receiver to the plate is given by

$$R_{re_max} = \left(\frac{\tan \theta + \cot(\beta - \theta)}{1 + \tan(\beta - 3\theta) \cot(\beta - \theta)} - 0.5 \tan \theta \right) D. \tag{8}$$

Simulations were performed to demonstrate the effects of these reflections occurring in the transmitter and receiver sides. For the first simulation, $\alpha = 15^\circ$, and $R_{tr_max} = 70$ mm, so it meets the requirement in (7) when $R = 30$ mm. The new incidence angle α' is 45° according to (6). Snapshots of the wave fields in the plate and air domains are shown in Fig. 9 at different times. It can be seen in Fig. 9(a) that there is a strong planar wave emanating from the front face of the transducer, plus two lower-amplitude arcuate edge waves emanating from the transducer edges, as would be expected from plane piston behaviour. At a time of $100 \mu s$, the planar pressure wave enters the plate at the original incidence angle of 15° , and most of the wave reflects. The starting point of the A_0 mode is seen to be at about $X = -10$ to -20 mm as the left-hand side of the transmitter is closer to the plate. Fig. 9(b) shows that the pressure wave reflects again at the surface of the transmitter after $200 \mu s$. The Lamb wave excited in the plate initially in Fig. 9(a) has now travelled a distance of about 70 mm (this is the A_0 mode at 700 m/s in $100 \mu s$). In Fig. 9(c), a new Lamb wave is excited by the reflected planar pressure wave at a time of approximately $300 \mu s$. Comparing the intensity scales in Fig. 9(a) and (c) it is clear that the reflected pressure wave has excited a higher intensity Lamb wave in the plate due to the change in angle of incidence. ($\alpha' = 3\alpha = 45^\circ$).

For the second simulation considering the reflection occurring in the receiver side, $\beta = 50^\circ$, $\theta = 15^\circ$, and $R_{re_max} = 52$ mm. This also meets the requirement in (8) when $R = 30$ mm. Snapshots of the wave fields in the plate and air domains are shown in Fig. 10 at different times. It can be seen in Fig. 10(a) that at a time of $520 \mu s$, the leaky Lamb wave reaches the receiver at an oblique angle, and most of the wave reflects. Fig. 10(b) shows the reflected wave reflects again at the surface of the plate at about $620 \mu s$. In Fig. 10(c), the reflected wave from the plate arrives at the receiver at $720 \mu s$ at a smaller incidence angle. From the intensity scales which indicate the pressure of the wave field, the leaky Lamb wave in the air gap still has significant energy after two reflections, as expected. The receiver will then detect a stronger signal from the second signal (reflected) than the first one (direct) because more of the surface normal component of the wave can impact on the receiver surface when the wave front angle matches the receiver angle of 15° .

These simulations suggest that specific signals with different amplitudes due to the different reflections between the plate and both the transmitters and receivers should be detected, depending on the angles of incidence. Thus, simulations containing four configurations of transmitter and receiver were performed, and the simulated received signals are shown in Figs. 11–14. In the first simulation, the angles of the transmitter and the receiver were both 50° . This configuration at the correct distance R eliminates any reflection and is used as a reference. In the next two simulations, the angle of the transmitter and the receiver were alternately changed to 15° respectively, so that a reflection occurred first on the transmitter side and then on the receiver side. In the last simulation, the angles of the transmitter and the receiver were both changed to 15° simultaneously, and reflections occurred in both sides. Additionally, the receiver will be most sensitive to the antisymmetric mode at an angle of 50° , and most sensitive to the symmetric mode at the angle of 15° according to the wave field in Fig. 5, and Snell's Law.

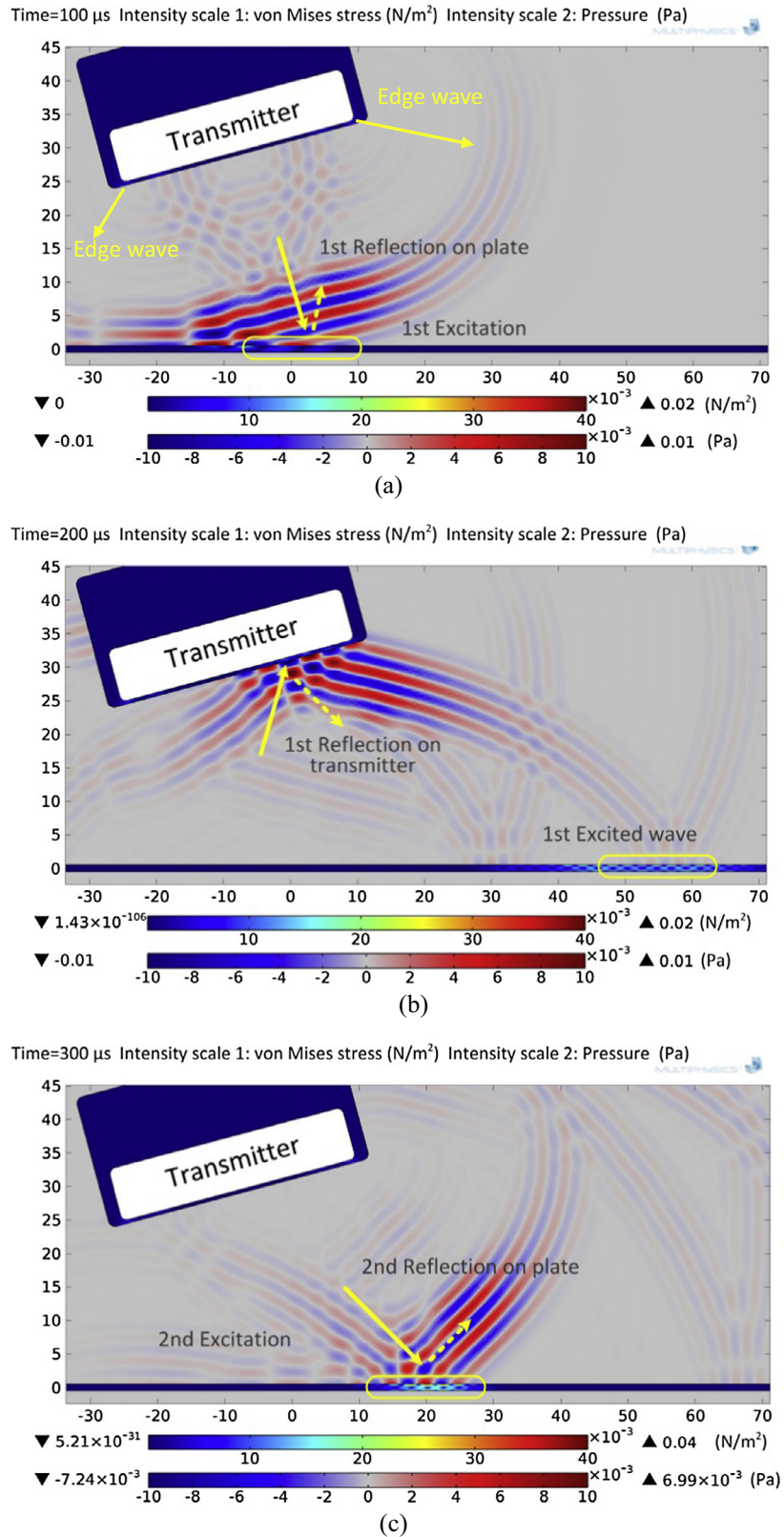


Fig. 9. Visualisation of Lamb wave excitation. (a) First excitation at a time of 100 μs . (b) Reflection by the transmitter at a time of 200 μs . (c) Second excitation by the reflected wave at a time of 300 μs .

3.3.1. Transmitter at 50°, receiver at 50°

From Fig. 11(a), an obvious signal starts at about 490 μs and reaches its maximum at about 550–560 μs . This signal is attributed

to the first direct A_0 excitation, and is denoted by $A_{0(T0,R0)}$ (the subscripts in parentheses refer to the number of times the wave is reflected by the transmitter and the receiver, respectively).

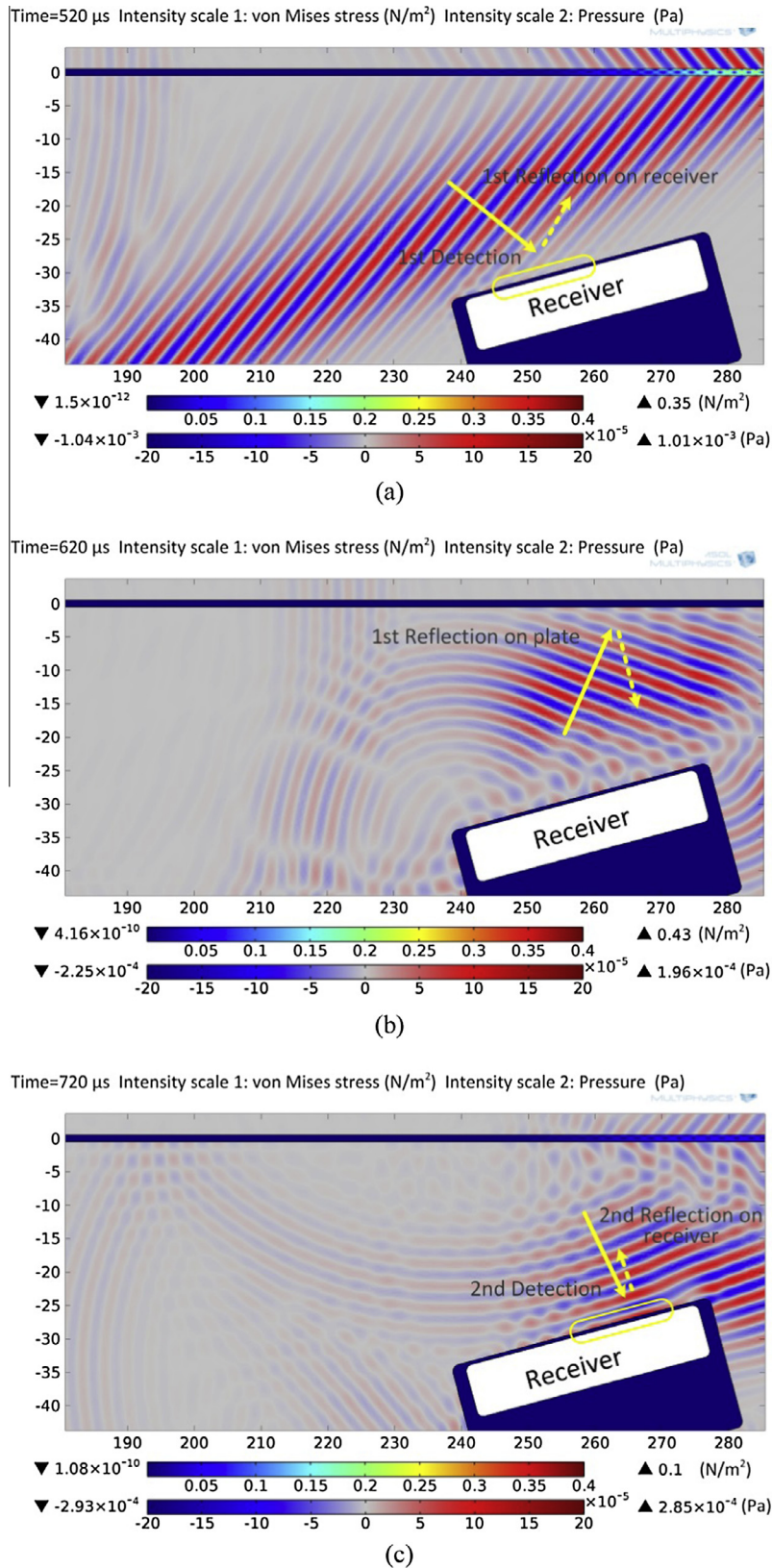


Fig. 10. Visualisation of leaky Lamb wave detection. (a) First detection at a time of 520 μs . (b) Reflection by the plate at a time of 620 μs . (c) Second detection by the reflected wave at a time of 720 μs .

According to the propagation paths of the signals shown in Fig. 11(b), on the transducer centrelines between the entry and exit points X_{in} and X_{out} the signals should have travelled a total path

of $2R = 60 \text{ mm}$ in the air at 340 m/s and $L = 250 \text{ mm}$ in the plate at 700 m/s, giving a total propagation time of 534 μs . However, due to the 38 mm width of the transducers and diffraction, the

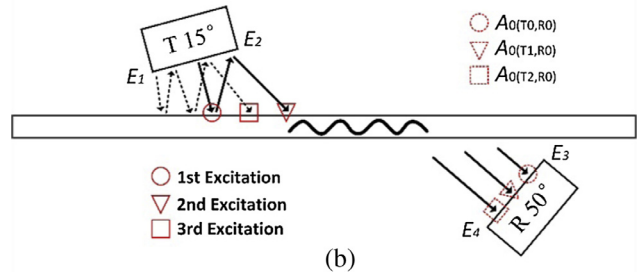
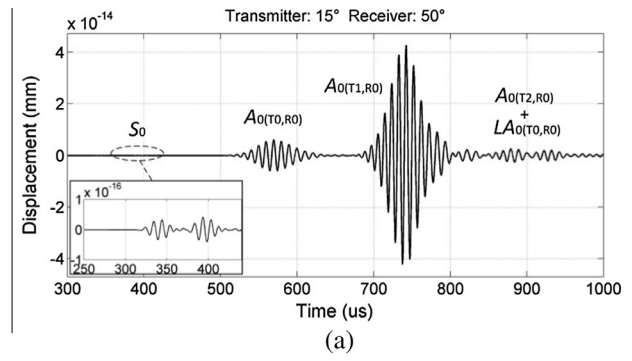
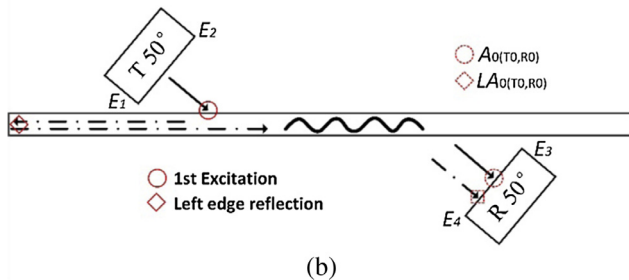
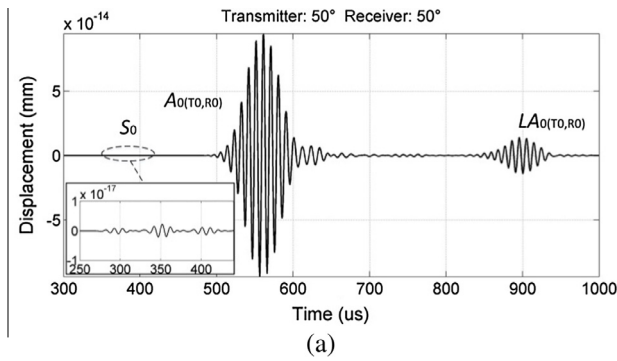


Fig. 11. (a) Simulation signals collected by the receiver for configuration: transmitter: 50°, receiver: 50°. (b) Schematic diagram of the measurable signals.

Fig. 12. (a) Simulation signals collected by the receiver for configuration: transmitter: 15°, receiver: 50°. (b) Schematic diagram of the measurable signals.

paths of the wave from the left and right extremes of the transducer faces will be slightly different and the A_0 mode generation and arrival will be spread out over a range of times, independent of any dispersion. The signal transmitted by the left hand edge E_1 and received by the right hand edge E_3 will have the shortest path in air at 340 m/s of only 14.8 mm and the longest path in the plate at 700 m/s of 309.1 mm, giving a theoretical minimum overall propagation time of 485 μ s, assuming no dispersion. The signal transmitted by the right hand edge E_2 and received by the left hand edge E_4 will have the longest path in air at 340 m/s of 105.3 mm and the shortest path in the plate at 700 m/s of 190.9 mm, giving a theoretical maximum overall propagation time of 582.4 μ s, again assuming no dispersion. Therefore, the analytical arrival times of the first A_0 wave closely match the values obtained from the simulations.

The signal $LA_{0(T0,R0)}$ which arrives between 850 and 950 μ s is the part of the A_0 Lamb wave that propagates to the left (hence LA_0) extremity of the plate and reflects: from the entry point X_{in} , this has an additional propagation path $2L_1$ of 300 mm in the plate at 700 m/s, and the theoretical additional propagation time for this A_0 Lamb wave mode in the plate is 428.6 μ s. Again, due to the width of the transducers, its generation and arrival will be spread out over a range of times between 829 μ s and 1095 μ s independent of any dispersion. This is again in good agreement to the values from simulation.

In this scenario, the S_0 Lamb wave is too weak to observe easily as neither the transmitter or the receiver are inclined at the correct angle of 15°, but the S_0 mode is still present as can be seen if the vertical scale is enhanced, as shown in the inset in Fig. 11(a). This S_0 signal is produced only by the lower-amplitude annular edge waves emanating from the two edges E_1 and E_2 of the transmitter as these radiate some energy at all angles, as can be seen by the arcuate wavefronts in Fig. 9(a) and would be expected by basic diffraction theory. The two separate edge waves from the transmitter are then detected individually by the two separate edges of the receiver, so that four separate arrivals may be expected. But there are only three propagation paths of different lengths, so only three

S_0 signals are seen because two of the signals have travelled along identical propagation paths, and are superimposed. This may be explained as follows, referring to Fig. 11(a) and (b). The first S_0 signal arriving at about 270 μ s in the inset in Fig. 11(a) is the first edge wave from the transmitter edge E_1 nearest the plate detected by the edge E_3 of the receiver nearest the plate, which has the shortest overall propagation path in air at 340 m/s, and the longest path in the plate at 1380 m/s. The second S_0 signal to arrive at about 325 μ s is a combination of two signals: the first edge wave from the nearest transmitter edge E_1 detected by the furthest edge E_4 of the receiver, plus the second edge wave from the furthest transmitter edge E_2 detected by the nearest edge E_3 of the receiver. These two signals have propagation paths of identical length, and so arrive at the same time due to the symmetry of the simulation. The third S_0 signal to arrive at about 380 μ s is the second edge wave from the furthest transmitter edge E_2 detected by the furthest edge E_4 of the receiver, which has the longest overall propagation path in air and the shortest path in the plate. This also explains why the second combined S_0 signal is bigger than the other two. Note also that the overall S_0 amplitude seen in the inset in Fig. 11(a) is quite low at $\pm 1 \times 10^{-17}$ mm full scale, as neither transducer is inclined at the optimum angle of 15° for the S_0 mode. The separation between these three S_0 signals of approximately 55 μ s matches well with the expected differences in the respective theoretical paths in air at 340 m/s and in the plate at 1380 m/s. The annular waves from transmitter edges E_1 and E_2 also produce the small signal between 700 and 800 μ s after they are reflected in the air gap from the plate surface back towards the transmitter and back towards the plate surface again.

3.3.2. Transmitter at 15°, receiver at 50°

In Fig. 12(a), the leaky Lamb wave from the first direct A_0 excitation which is marked as $A_{0(T0,R0)}$ reaches its maximum at a similar time to that in Fig. 11(a). The overall amplitude of this A_0 wave is now much smaller as the transmitter angle is now 15°, optimised for the S_0 mode, rather than 50° for the A_0 mode. Notice, however, that a strong signal now arrives between 700 and 800 μ s, due to a second excitation originating from the first air gap

reflection between the transmitter and the plate as shown in Fig. 9(c), which is marked as $A_{0(T1,RO)}$. The theoretical time delay in the additional path of 60 mm in the air is $176 \mu\text{s}$, so the total propagation time is now $176 \mu\text{s} + 534 \mu\text{s} = 710 \mu\text{s}$. Fig. 9(c) also shows that this second A_0 excitation in the plate would be much stronger than the first. Hence, the signals in Fig. 12(a) could easily be misinterpreted, i.e. the small $A_{0(TO,RO)}$ signal could be seen as the S_0 mode and the larger $A_{0(T1,RO)}$ signal as the $A_{0(TO,RO)}$ mode, but travelling with the wrong group velocities. Also, a small signal marked as $A_{0(T2,RO)}$ arrives from a third excitation due to a second reflection between the transmitter and the plate and interferes with the $LA_{0(TO,RO)}$ signal between $850 \mu\text{s}$ and $950 \mu\text{s}$.

In this case, the S_0 mode and $LA_{0(TO,RO)}$ wave are only weakly present, but again the S_0 mode is visible if the vertical scale is enhanced, as shown by the insert in Fig. 12(a). This time there are two S_0 signals, as there is a single plane wave from the transmitter at 15° which is detected separately by each of the two edges of the receiver only, at approximately $315 \mu\text{s}$ and $370 \mu\text{s}$, as the main plane surface of the receiver is inclined at 50° . For the first signal, the propagation path in the air is 35 mm, the path in the plate is 285 mm, and the theoretical time $308 \mu\text{s}$; for the second signal, the propagation path in the air is 65 mm, the path in the plate is 253 mm, and the theoretical time $374 \mu\text{s}$ which closely match the simulated values. The model also confirmed that in this scenario shown in Fig. 5, a single S_0 signal was propagating in the plate. Note also that the S_0 amplitude is 10 times higher than in Fig. 11(a) at $\pm 1 \times 10^{-16}$ mm full scale, as now one transducer is at the optimum angle of 15° for the S_0 mode (the transmitter). The propagation paths of the signals are shown in Fig. 12(b) schematically.

3.3.3. Transmitter at 50° , receiver at 15°

Fig. 13(a) shows a similar waveform to Fig. 12(a), but the mechanism is quite different because there is no extra excitation due to an air gap reflection between the transmitter and the plate in this case. The first obvious signal $A_{0(TO,RO)}$ has a similar amplitude to that in Fig. 12 because the transmitter is now at the optimum A_0 angle of 50° and the receiver is at 15° . This wave is then reflected

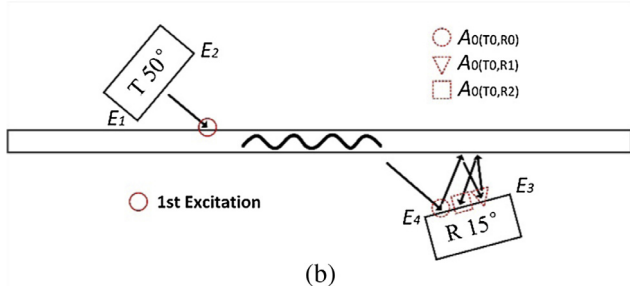
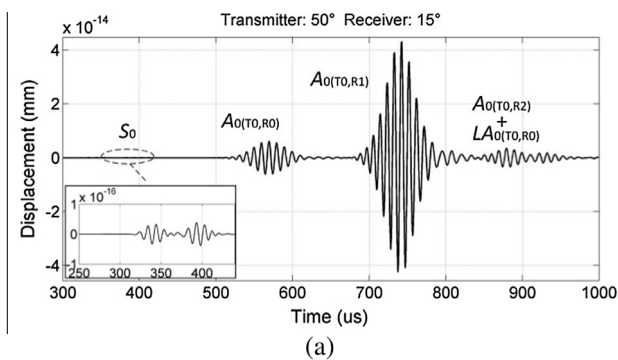


Fig. 13. (a) Simulation signals collected by the receiver for configuration: transmitter: 50° , receiver: 15° . (b) Schematic diagram of the measurable signals.

between the receiver and the plate, and it reaches the receiver a second time at a different angle (20°) which is marked as $A_{0(TO,R1)}$. It has been illustrated already in Fig. 10(c) that the receiver can collect more energy if the wave front is at the same angle as the receiver, thus a strong signal is detected between 700 and $800 \mu\text{s}$ with a theoretical time delay in the additional path of 60 mm in the air of $176 \mu\text{s}$ as before. As a part of the wave is reflected in the air gap between the receiver and the plate, another weaker signal $A_{0(TO,R2)}$ interfered with the $LA_{0(TO,RO)}$ is detected after the same time delay as before.

The S_0 mode and $LA_{0(TO,RO)}$ signal are only weakly present as before. Again, there are only two S_0 signals here but unlike in Fig. 12(a), they are the two signals from the two edges of the transmitter, containing a component inclined at 15° , which are each received only once by the full planar surface of the receiver, also inclined at 15° . The model confirmed that in this scenario, there were two distinct S_0 signals propagating in the plate. Note also that the signal shape and the total amplitude are virtually identical to Fig. 12(a) as again only one transducer is at the optimum angle of 15° for the S_0 mode (the receiver). The first S_0 signal to arrive in Fig. 13(a) is at the same time as that in Fig. 12(a), as the paths are of identical length. The propagation paths of the signals are shown in Fig. 13(b) schematically.

3.3.4. Transmitter at 15° , receiver at 15°

It can be seen in Fig. 14(a) that the leaky S_0 Lamb wave can now be clearly detected by using the transmitter and the receiver both at 15° . The corresponding signal between 350 and $400 \mu\text{s}$ is marked as S_0 , with a centreline path in the air of 60 mm and a path in the plate of 250 mm giving a theoretical time of $358 \mu\text{s}$. However, with this configuration, the $A_{0(TO,RO)}$ wave from the first excitation is very weak, so it is hard to detect it at the receiver angle of 15° . From Figs. 12(a) and 13(a), it is known that the signal $A_{0(T1,RO)} + A_{0(TO,R1)}$ between 700 and $800 \mu\text{s}$ is composed of the wave from the first reflection at the transmitter side and the wave from the first reflection at the receiver side. Finally, because the second excitation generates a strong A_0 Lamb wave mode at 45°

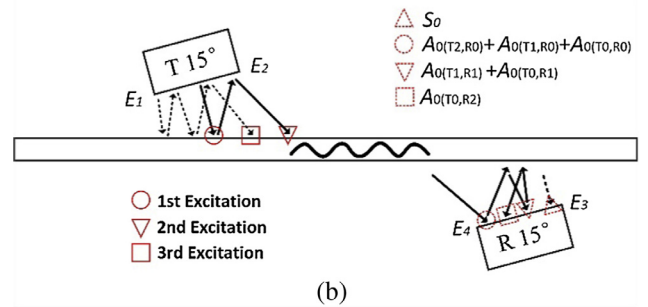
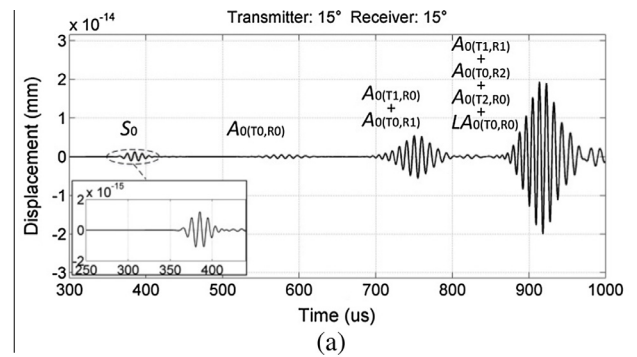


Fig. 14. (a) Simulation signals collected by the receiver for configuration: transmitter: 15° , receiver: 15° . (b) Schematic diagram of the measurable signals.

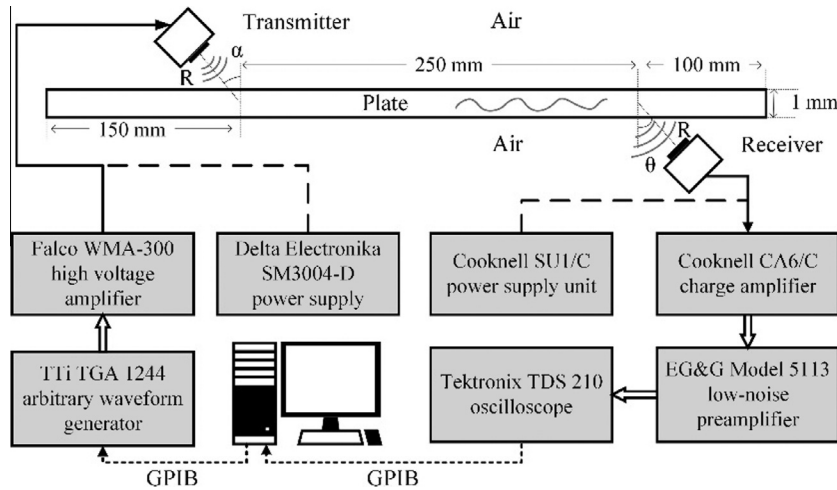


Fig. 15. Schematic diagram of experimental set-up.

and the receiver mainly collects energy from the reflected wave at 15° , a strong signal is seen between 850 and 950 μs . This signal is composed of four parts: $A_{0(T1,R1)} + A_{0(T2,R0)} + A_{0(T0,R2)} + LA_{0(T0,R0)}$, and most of its energy comes from $A_{0(T1,R1)}$. There is now only one S_0 signal as the planar wave from the transmitter at 15° is received by the full planar surface of the receiver at 15° . The presence of only a single S_0 signal in the plate was confirmed previously by the model in Fig. 5. Note also that the S_0 amplitude is the highest in this simulation at $\pm 2 \times 10^{-15}$ mm full scale, as now both transducers are at the optimum angle of 15° for the S_0 mode. The propagation paths of the signals are shown in Fig. 14(b) schematically.

These simulations show that care must be taken when analysing leaky Lamb wave signals in an air-coupled system, particularly if the signals are noisy. If the air paths, transducer angles and subsequent reflections are not well understood, then the $A_{0(T0,R0)}$ signal in Figs. 12(a) and 13(a) could easily be misinterpreted as the S_0 mode. Similarly, the $A_{0(T1,R0)}$ and $A_{0(T0,R1)}$ signals, as they are the largest, could be misinterpreted as the $A_{0(T0,R0)}$ signal. This would lead to a significant error in measurement of phase and group velocities in air-coupled NDE using leaky Lamb waves, if the properties of the plate and speeds of sound were not known *a priori*.

It should be noted that attenuation of the signals in the air was not included in the COMSOL model to reduce the significant additional computation time that would be required. The attenuation coefficient in air at frequencies of 100 kHz or less is well-known to be below 1 dB/m [24] and the total propagation paths in air, even for multiple reflections were of the order of 0.1 m or less, so it was not necessary to add this significant additional computational complexity to the COMSOL model to demonstrate the effect of the air gap reflections generating the additional delayed Lamb wave signals. In addition, the model and the subsequent experiments were set up so that the propagation paths in air were of constant length irrespective of the angle of inclination of the transducers, which meant that any attenuation would be the same in all the scenarios investigated.

4. Experimental measurement

To verify the model experimentally, a windowed sinusoid signal was first generated using MATLAB before being sent to a TTI TGA 1244 arbitrary waveform generator via a GPIB interface. The signal, similar to the one used in the simulation, was then amplified by a Falco WMA-300 high voltage amplifier, and combined with a bias voltage of +150 V generated by a Delta Elektronika SM3004-D

power supply. After that, the signal was sent to a 38 mm diameter SensComp series 600 air-coupled capacitive ultrasonic transducer. The receiver transducer was identical to the transmitter transducer, but was connected to a Cooknell CA6/C charge amplifier powered by a Cooknell SU1/C power supply unit with integrated 100 V dc bias. The signal was further amplified and band-pass filtered from 30 to 300 kHz by an EG&G Model 5113 low-noise preamplifier. A Tektronix TDS 210 oscilloscope with a sample rate of 2.5 MHz was then used to acquire the signal for post processing.

The experimental set-up of the two-sided pitch-catch configuration is shown in Fig. 15. The polycarbonate plate used in the experiments was 500 mm \times 500 mm \times 1 mm in size and clamped in a vertical plane to prevent any deflection under its own weight. The transmitter was placed at a radius R of 30 mm from the entry point, and the incidence angle varied from 10° to 55° . The distance from the entry point and the leaky point was $L = 250$ mm as in the simulations. The receiver was aimed at the leaky point at a distance of 30 mm at different angles. All signals were averaged 128 times to further reduce noise.

Four experimental configurations of transmitter and receiver were used as in the simulations: (a) Reference (no reflections), transmitter: 50° , receiver: 50° ; (b) Reflection at transmitter side only, transmitter: 15° , receiver: 50° ; (c) Reflection at receiver side only, transmitter: 50° , receiver: 15° ; (d) Reflection at both sides, transmitter: 15° , receiver: 15° . The signals are shown in Fig. 16 (a) to (d), respectively. The experimental signals were also cross-correlated with the transmitted signal (windowed 5 cycle sinusoid) to clearly show the modes and propagation times as shown in Fig. 17.

From Figs. 16 and 17, it can be seen that there is good agreement between the signals obtained in the experiments compared to those from the simulations, with minor differences due to the difficulties of practical experimental alignment, differences in the theoretical and actual properties of the polycarbonate used, and non-ideal plane piston transducer behaviour. 1 mm error in the alignment produces a 3 μs error in the air gap wave propagation time and a 1.5 μs error in the A_0 wave propagation time in the plate. It should also be noticed that the obvious $A_{0(T0,R0)}$ and $A_{0(T1,R0)}$ waves in Fig. 16(b) and (c) could easily be mistaken for the S_0 and A_0 waves, particularly if the wave velocities in the plate are not known *a priori*. The S_0 mode can only be detected clearly in Figs. 16(d) and 17(d), due to the low SNR of the signals. In addition, the S_0 modes are obscured by the noise in Fig. 16(b) and (c), making the misinterpretation of the $A_{0(T0,R0)}$ signal as the S_0 mode more likely. Thus, it is important to check the air paths and arrival times

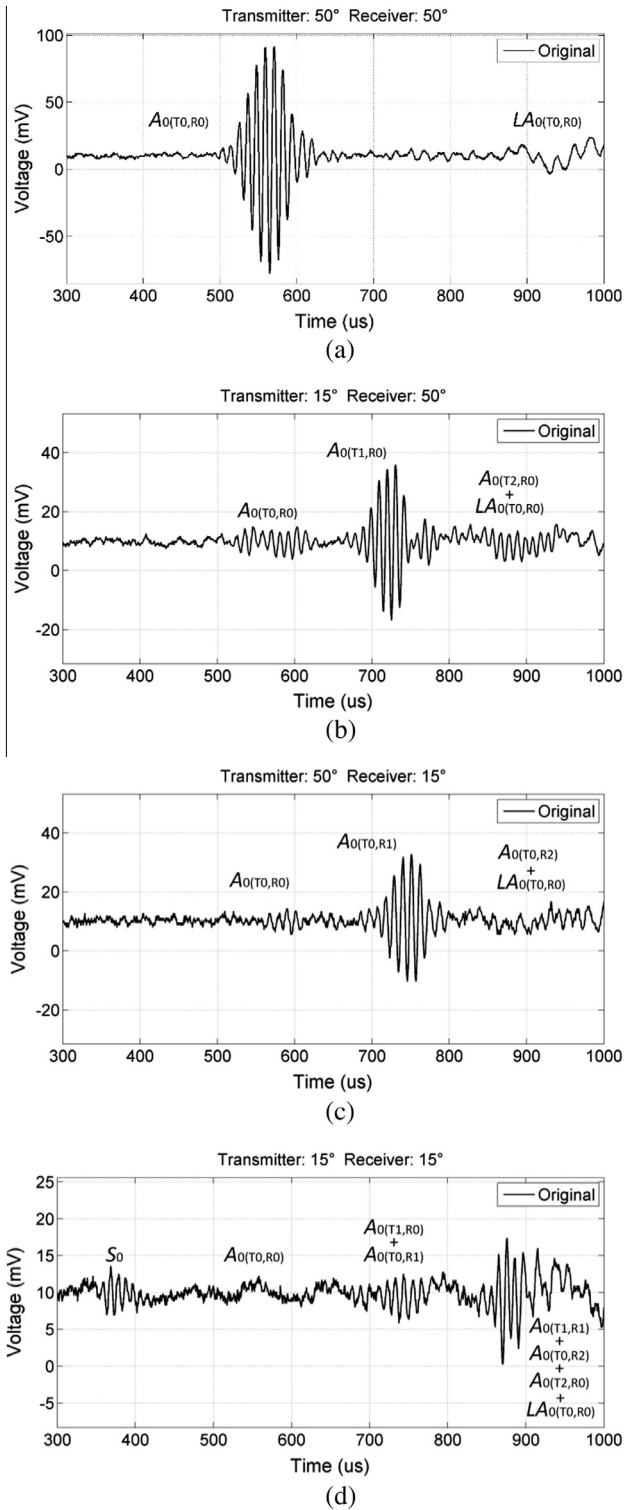


Fig. 16. Experimentally measured signals collected by the receiver for four configurations. (a) Transmitter: 50°, receiver: 50°. (b) Transmitter: 15°, receiver: 50°. (c) Transmitter: 50°, receiver: 15°. (d) Transmitter: 15°, receiver: 15°.

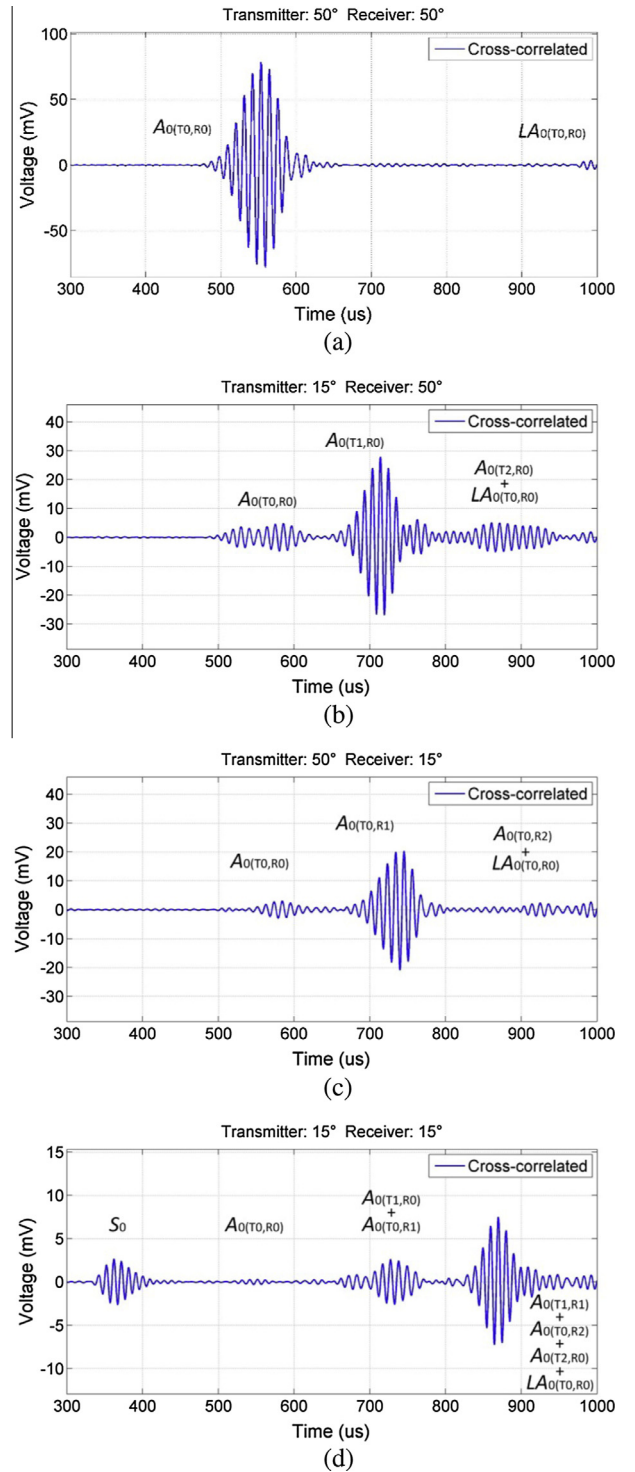


Fig. 17. Experimental measurement signals cross-correlated with the transmitted signal for four configurations. (a) Transmitter: 50°, receiver: 50°. (b) Transmitter: 15°, receiver: 50°. (c) Transmitter: 50°, receiver: 15°. (d) Transmitter: 15°, receiver: 15°.

for each signal, to correctly identify the different waves, for which the multiphysics model is extremely useful.

In order to confirm the received modes, a time–frequency analysis using a wavelet transform was applied to show any dispersion of the leaky Lamb waves, and the result is shown in Fig. 18. The signal in the antisymmetric mode was chosen from the first

configuration where the transmitter angle and the receiver angle are both 50°. The dashed arrow indicates the trend of different frequency components varying with time. In the antisymmetric mode, the wave components with higher frequencies (100–110 kHz) move faster than those with lower frequencies (70–80 kHz), confirming that this is the dispersive A_0 Lamb wave propagating in the 1 mm plate.

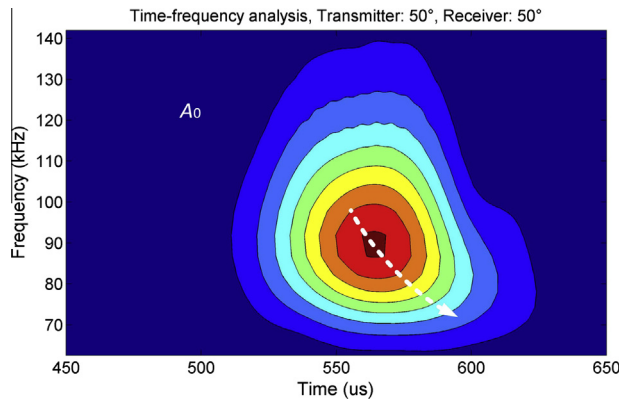


Fig. 18. Time–frequency analysis for the collected experimental signal.

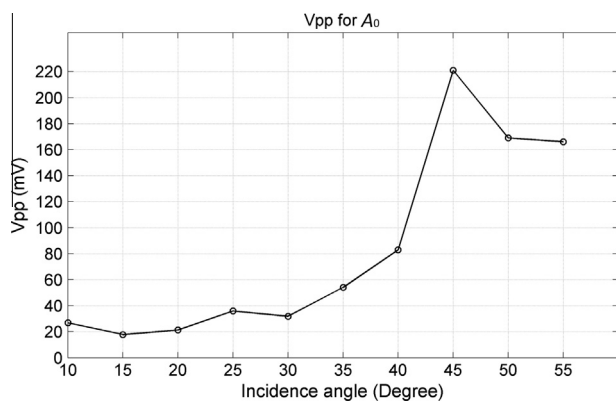


Fig. 19. Peak-to-peak amplitudes dependency versus the incidence angle for experiments (A_0 mode only).

Finally, to experimentally verify the intensity of the leaky Lamb waves at different incidence angles, the transmitter was also adjusted to different incidence angles similar to the previous simulations. Received peak-to-peak amplitudes for the experimental signals are shown in Fig. 19. It can be seen that leaky Lamb waves in the A_0 mode were best received when a 45° incidence angle was used, while the weakest signal was obtained at an angle of incidence of 15° . These correspond well with the angles of maximum and minimum attenuation expected from the simulations shown earlier Fig. 7, with minor differences of 5° or less occurring due to the practical difficulties of precise transducer alignment.

5. Conclusions

In this work, a multiphysics model using finite element methods (COMSOL) was implemented successfully to visualise and predict the effects of air–gap reflections of both the bulk waves and leaky Lamb waves used to investigate thin plates with non-contact air-coupled ultrasonic transducers. As the size of many air-coupled transducers tends to be large due to the wavelengths of ultrasound in air and poor energy conversion efficiency, the reflections that may exist between the plate and the transducer on both the transmitter and receiver sides of the system have been shown, at certain angles of incidence, to produce additional Lamb wave modes in the plate under test.

This study also demonstrated that care must be taken when interpreting the received signals. At certain angles, the reflected signals produced Lamb waves that were much higher in amplitude than the directly generated signals, which could lead to confusion

in identifying the correct mode if the phase and group velocity in the plate was not known *a priori*. The multiphysics model allowed the correct modes to be identified, including the secondary signals produced by the air gap reflections, and the simulations were in good agreement with the experimental results. This study also demonstrated that a multiphysics modelling approach provides an effective way of accurately predicting the output of an air-coupled ultrasonic non-contact inspection system using leaky Lamb waves, and provided significant guidance for interpretation of the measured signals and the overall design of the inspection system.

Acknowledgements

The authors wish to express their gratitude for the financial support for Zichuan Fan under the State Scholarship Fund from the China Scholarship Council (CSC) to study at University College Cork. The work was also supported by Science Foundation Ireland (SFI) under the Research Frontiers Programme, grant 11/RFP.1/ECE/3119.

References

- [1] W.A. Grandia, C.M. Fortunko, NDE applications of air-coupled ultrasonic transducers, in: Proc. IEEE Ultrason. Symp., 1995, pp. 697–709.
- [2] S.P. Kelly, R. Farlow, G. Hayward, Application of through-air ultrasound for rapid NDE scanning in the aerospace industry, IEEE Trans. Ultrason. Ferroelectr. Freq. Contr. 43 (1996) 581–591.
- [3] M. Castaings, P. Cawley, R. Farlow, G. Hayward, Single sided inspection of composite materials using air coupled ultrasound, J. Nondestruct. Eval. 17 (1998) 37–45.
- [4] E. Blomme, D. Bulcaen, F. Declercq, P. Lust, Air-coupled ultrasonic evaluation of coated textiles, in: Proc. IEEE Ultrason. Symp., 2002, pp. 757–760.
- [5] T.H. Gan, D.A. Hutchins, D.R. Billson, D.W. Schindel, High-resolution air-coupled ultrasonic imaging of thin materials, IEEE Trans. Ultrason. Ferroelectr. Freq. Contr. 50 (2003) 1516–1524.
- [6] R.E. Green, Non-contact ultrasonic techniques, Ultrasonics 42 (2004) 9–16.
- [7] M. Luukkala, P. Heikkala, J. Surakka, Plate wave resonance – a contactless test method, Ultrasonics 9 (4) (1971).
- [8] W.M.D. Wright, D.W. Schindel, D.A. Hutchins, Studies of laser-generated ultrasound using a micromachined silicon electrostatic transducer in air, J. Acoust. Soc. Am. 95 (5) (1994) 2567–2575.
- [9] M. Castaings, P. Cawley, The generation, propagation, and detection of Lamb waves in plates using air-coupled ultrasonic transducers, J. Acoust. Soc. Am. 100 (5) (1996) 3070–3077.
- [10] A. Safaeinili, O.I. Lobkis, D.E. Chimenti, Air-coupled ultrasonic estimation of viscoelastic stiffnesses in plates, IEEE Trans. Ultrason. Ferroelectr. Freq. Contr. 43 (6) (1996) 1171–1179.
- [11] W. Wright, D. Hutchins, D. Jansen, D. Schindel, Air-coupled Lamb wave tomography, IEEE Trans. Ultrason. Ferroelectr. Freq. Contr. 44 (1) (1997) 53–59.
- [12] A. Safaeinili, O.I. Lobkis, D.E. Chimenti, Quantitative materials characterization using air-coupled leaky Lamb waves, Ultrasonics 34 (2–5) (1996) 393–396.
- [13] M. Castaings, B. Hosten, Lamb and SH waves generated and detected by air-coupled ultrasonic transducers in composite material plates, NDT & E Int. 34 (2001) 249–258.
- [14] R. Kazys, A. Demcenko, E. Zukauskas, L. Mazeika, Air-coupled ultrasonic investigation of multi-layered composite materials, Ultrasonics 44 (2006) 819–822.
- [15] C. Ramadas, K. Balasubramaniam, M. Joshi, C.V. Krishnamurthy, Interaction of the primary anti-symmetric Lamb mode (A_0) with symmetric delaminations: numerical and experimental studies, Smart Mater. Struct. 18 (8) (2009), <http://dx.doi.org/10.1088/0964-1726/18/8/085011>.
- [16] B. Hosten, C. Biateau, Finite element simulation of the generation and detection by air-coupled transducers of guided waves in viscoelastic and anisotropic materials, J. Acoust. Soc. Am. 123 (4) (2008) 1963–1971.
- [17] S. Delrue, K. Van Den Abele, E. Blomm, J. Deveugele, P. Lust, O.B. Matar, Two-dimensional simulation of the single-sided air-coupled ultrasonic pitch-catch technique for non-destructive testing, Ultrasonics 50 (2) (2010) 188–196.
- [18] G. Dobie, A. Spencer, K. Burnham, G.S. Pierce, K. Worden, W. Galbraith, G. Hayward, Simulation of ultrasonic Lamb wave generation, propagation and detection for a reconfigurable air coupled scanner, Ultrasonics 51 (2011) 258–269.
- [19] A. Vilpisauskas, R. Kazys, Numerical investigation of air coupled generation of Lamb waves in isotropic plates, Elektron. Elektrotechn. 20 (1) (2014) 33–36.
- [20] I.A. Viktorov, Rayleigh and Lamb Waves: Physical Theory and Applications, Plenum, New York, 1967.
- [21] COMSOL Multiphysics User's Guide, Version 4.4, 2013.

- [22] R. Courant, K.O. Friedrichs, H. Lewy, On the partial difference equations of mathematical physics, *IBM J.* 11 (1956) 215–234.
- [23] J.J. Ditre, K. Rajana, An experimental study of the angular dependence of lamb waves excitation, *J. Sound Vib.* 204 (5) (1997) 755–768.
- [24] H.E. Bass, Absorption of sound by the atmosphere, in: W.P. Mason, R.N. Thurston (Eds.), *Physical Acoustics: Principles and Methods*, vol. XVII, Academic Press, Orland, 1984.